Draft version November 28, 2016
Preprint typeset using LaTeX style emulateapj v. 5/2/11

arXiv:1611.08052v1 [astro-ph.HE] 24 Nov 2016

A SEARCH FOR KILONOVAE IN THE DARK ENERGY SURVEY

Z. Doctor[1,2,3], R. Kessler[1,4], H. Y. Chen[1,4], B. Farr[1,2,5], D. A. Finley[6], R. J. Foley[7], D. A. Goldstein[8,9], D. E. Holz[1,2,4,5], A. G. Kim[9], E. Morganson[10], M. Sako[11], D. Scolnic[1], M. Smith[12], M. Soares-Santos[6], H. Spinka[13], T. M. C. Abbott[14], F. B. Abdalla[15,16], S. Allam[6], J. Annis[6], K. Bechtol[17], A. Benoit-Lévy[18,15,19], E. Bertin[18,19], D. Brooks[15], E. Buckley-Geer[6], D. L. Burke[20,21], A. Carnero Rosell[22,23], M. Carrasco Kind[24,10], J. Carretero[25,26], C. E. Cunha[20], C. B. D'Andrea[27,12], L. N. da Costa[22,23], D. L. DePoy[28], S. Desai[29], H. T. Diehl[6], A. Drlica-Wagner[6], T. F. Eifler[30], J. Frieman[6,1], J. García-Bellido[31], E. Gaztanaga[25], D. W. Gerdes[32], R. A. Gruendl[24,10], J. Gschwend[22,23], G. Gutierrez[6], D. J. James[33,14], E. Krause[20], K. Kuehn[34], N. Kuropatkin[6], O. Lahav[15], T. S. Li[6,28], M. Lima[35,22], M. A. G. Maia[22,23], M. March[11], J. L. Marshall[28], F. Menanteau[24,10], R. Miquel[36,26], E. Neilsen[6], R. C. Nichol[27], B. Nord[6], A. A. Plazas[30], A. K. Romer[37], E. Sanchez[38], V. Scarpine[6], M. Schubnell[32], I. Sevilla-Noarbe[38], R. C. Smith[14], F. Sobreira[22,39], E. Suchyta[40], M. E. C. Swanson[10], G. Tarle[32], A. R. Walker[14], W. Wester[6]

(DES Collaboration)

[1] Kavli Institute for Cosmological Physics, University of Chicago, Chicago, IL 60637, USA
[2] Department of Physics, University of Chicago, Chicago, IL 60637, USA
[3] NSF GRFP Fellow
[4] Department of Astronomy and Astrophysics, University of Chicago, Chicago, IL 60637, USA
[5] Enrico Fermi Institute, University of Chicago, Chicago, IL 60637, USA
[6] Fermi National Accelerator Laboratory, P. O. Box 500, Batavia, IL 60510, USA
[7] Department of Astronomy and Astrophysics, University of California, Santa Cruz, CA 95064, USA
[8] Department of Astronomy, University of California, Berkeley, 501 Campbell Hall, Berkeley, CA 94720, USA
[9] Lawrence Berkeley National Laboratory, 1 Cyclotron Road, Berkeley, CA 94720, USA
[10] National Center for Supercomputing Applications, 1205 West Clark St., Urbana, IL 61801, USA
[11] Department of Physics and Astronomy, University of Pennsylvania, Philadelphia, PA 19104, USA
[12] School of Physics and Astronomy, University of Southampton, Southampton, SO17 1BJ, UK
[13] Argonne National Laboratory, 9700 South Cass Avenue, Lemont, IL 60439, USA
[14] Cerro Tololo Inter-American Observatory, National Optical Astronomy Observatory, Casilla 603, La Serena, Chile
[15] Department of Physics & Astronomy, University College London, Gower Street, London, WC1E 6BT, UK
[16] Department of Physics and Electronics, Rhodes University, PO Box 94, Grahamstown, 6140, South Africa
[17] LSST, 933 North Cherry Avenue, Tucson, AZ 85721, USA
[18] CNRS, UMR 7095, Institut d'Astrophysique de Paris, F-75014, Paris, France
[19] Sorbonne Universités, UPMC Univ Paris 06, UMR 7095, Institut d'Astrophysique de Paris, F-75014, Paris, France
[20] Kavli Institute for Particle Astrophysics & Cosmology, P. O. Box 2450, Stanford University, Stanford, CA 94305, USA
[21] SLAC National Accelerator Laboratory, Menlo Park, CA 94025, USA
[22] Laboratório Interinstitucional de e-Astronomia - LIneA, Rua Gal. José Cristino 77, Rio de Janeiro, RJ - 20921-400, Brazil
[23] Observatório Nacional, Rua Gal. José Cristino 77, Rio de Janeiro, RJ - 20921-400, Brazil
[24] Department of Astronomy, University of Illinois, 1002 W. Green Street, Urbana, IL 61801, USA
[25] Institut de Ciències de l'Espai, IEEC-CSIC, Campus UAB, Carrer de Can Magrans, s/n, 08193 Bellaterra, Barcelona, Spain
[26] Institut de Física d'Altes Energies (IFAE), The Barcelona Institute of Science and Technology, Campus UAB, 08193 Bellaterra (Barcelona) Spain
[27] Institute of Cosmology & Gravitation, University of Portsmouth, Portsmouth, PO1 3FX, UK
[28] George P. and Cynthia Woods Mitchell Institute for Fundamental Physics and Astronomy, and Department of Physics and Astronomy, Texas A&M University, College Station, TX 77843, USA
[29] Department of Physics, IIT Hyderabad, Kandi, Telangana 502285, India
[30] Jet Propulsion Laboratory, California Institute of Technology, 4800 Oak Grove Dr., Pasadena, CA 91109, USA
[31] Instituto de Física Teórica UAM-CSIC, Universidad Autonóma de Madrid, Cantoblanco, 28049 Madrid, Spain
[32] Department of Physics, University of Michigan, Ann Arbor, MI 48109, USA
[33] Astronomy Department, University of Washington, Box 351580, Seattle, WA 98195, USA
[34] Australian Astronomical Observatory, North Ryde, NSW 2113, Australia
[35] Departamento de Física Matemática, Instituto de Física, Universidade de São Paulo, CP 66318, CEP 05314-970, São Paulo, SP, Brazil
[36] Institució Catalana de Recerca i Estudis Avançats, E-08010 Barcelona, Spain
[37] Department of Physics and Astronomy, Pevensey Building, University of Sussex, Brighton, BN1 9QH, UK
[38] Centro de Investigaciones Energéticas, Medioambientales y Tecnológicas (CIEMAT), Madrid, Spain
[39] Universidade Federal do ABC, Centro de Ciências Naturais e Humanas, Av. dos Estados, 5001, Santo André, SP, Brazil, 09210-580
[40] Computer Science and Mathematics Division, Oak Ridge National Laboratory, Oak Ridge, TN 37831

(Dated: November 28, 2016)
Draft version November 28, 2016

ABSTRACT

The coalescence of a binary neutron star (BNS) pair is expected to produce gravitational waves (GW) and electromagnetic (EM) radiation, both of which may be detectable with currently available instruments. While GW searches for BNS mergers are ongoing, untriggered optical searches for BNS mergers have not been performed. We describe a search for a theoretically predicted r-process optical transient from these mergers, dubbed the "kilonova" (KN), using *griz* broadband data from the Dark Energy Survey Supernova Program (DES-SN). Some models predict KNe to be redder, shorter-lived, and dimmer than supernovae (SNe), but at present the event rate of KNe is poorly constrained. We simulate observations of KN and SN light curves with the Monte-Carlo simulation code `SNANA` to

[1] zdoctor@uchicago.edu

optimize selection requirements, determine search efficiency, and predict SN backgrounds. We also perform an analysis using fake point sources on images to account for anomalous efficiency losses from difference-imaging on bright low-redshift galaxies. Our analysis of the first two seasons of DES-SN data results in 0 events, and is consistent with our prediction of 1.1 ± 0.2 background events based on simulations of SNe. Given our simulation prediction, there is a 33% chance of finding 0 events in the data. Assuming no underlying galaxy flux, our search sets 90% upper limits on the KN volumetric rate of 1.0×10^7 Gpc^{-3}yr^{-1} for the dimmest KN model we consider (peak i-band absolute magnitude $M_i = -11.4$ mag) and 2.4×10^4 Gpc^{-3}yr^{-1} for the brightest ($M_i = -16.2$ mag). Accounting for efficiency loss from host galaxy Poisson noise, these limits are 1.1 times higher; accounting for anomalous subtraction artifacts on bright galaxies, these limits are ~ 3 times higher. While previous KN searches were based on triggered follow-up, this analysis is the first untriggered optical KN search and informs selection requirements and strategies for future KN searches and GW follow-up observations. Our upper limits on the KN rate are consistent with those measured by GW and gamma-ray burst searches.

1. INTRODUCTION

The recent detections by LIGO of gravitational waves (GW) from binary black hole mergers (Abbott et al. 2016c,a) have motivated searches for electromagnetic (EM) counterparts to gravitational waves (Abbott et al. 2016b; Annis et al. 2016; Soares-Santos et al. 2016; Cowperthwaite et al. 2016). Theoretical and numerical studies suggest that outflows of energetic neutron-rich material during a binary neutron star (BNS) merger enable r-process nucleosynthesis (e.g. Li and Paczyński 1998). The decay of these r-process elements results in isotropic thermal emission and is called a "kilonova" (KN). Metzger and Berger (2012) compared different EM counterparts of GW sources and concluded that the kilonova has promising detectability with current instruments. Observations of KNe could constrain models of neutron star mergers, and an accurate redshift measurement would allow GW measurements to be used as cosmological distance probes (Schutz 1986; Dalal et al. 2006). While properties of optical KN light curves remain uncertain, a number of models predict KNe to be dim ($M_i \sim -14$ mag), red ($i - z \sim 1$ mag), and short-lived ($\sim$1 week) (Barnes and Kasen 2013; Tanaka and Hotokezaka 2013; Metzger and Fernández 2014; Lippuner and Roberts 2015).

An interesting KN candidate was reported by Tanvir et al. (2013) and Berger et al. (2013). The candidate was first identified by the gamma ray burst GRB130613B, which triggered both the *Swift* Burst Alert Telescope and Konus-Wind. Following GRB130613B, the teams reported two epochs of Hubble Space Telescope observations in the V and H bands as well as optical observations with the Inamori Magellan Areal Camera and Spectrograph (IMACS) and the Low Dispersion Survey Spectrograph (LDSS3) on the Magellan Telescopes. At 9.4 days after the GRB, the source was found to have $M_H \sim -15.2$ mag and $M_V \gtrsim -13.3$ mag, indicating a red $V - H$ color $\gtrsim 1.9$ mag. Other r-process events possibly involving a neutron star have been reported in Jin et al. (2016) and Ji et al. (2016).

Here we describe an independent search for KNe from the first two seasons of data from the Dark Energy Survey supernova program (DES-SN) (Bernstein et al. 2012; Diehl et al. 2016) using the Dark Energy Camera (DECam: Flaugher et al. 2015). KN searches triggered by GRBs or GWs will be an integral part of GW multi-messenger astronomy, but here we use existing DES-SN data to search for KNe without an external trigger. With four optical broadband filters, 30-square-degree coverage in the supernova fields, and $\sim$1 week cadence in each filter with excellent depth per visit, the DES-SN sample is well-suited for a KN search. Light curve simulations of KNe and supernova (SN) backgrounds are used to inform the analysis and selection criteria that we apply to the DES-SN data sample to look for KNe. The KN simulations are based on spectral energy distributions (SED) resulting from radiation transport calculations of KN-merger models from Barnes and Kasen (2013) (hereafter BK13). These calculations fold in r-process element opacities using atomic data for heavy elements rather than approximating their opacities with that of iron. As a result, BK13 predict KN light curves that are dimmer, redder, and longer-lived than those predicted with iron opacities. These models are still highly uncertain, so our analysis reports volumetric rate limits for each KN model and over a wide range of absolute brightnesses.

We make a preliminary estimate of our potential KN sensitivity using two approximate calculations based on previously published results. Both approximations assume a KN peak i-band magnitude of $M_i \sim -14$ mag and 100% search efficiency within the DES-SN limiting magnitudes and sky areas described in § 2. The first approximation assumes an optimistically large KN rate given by the LIGO 90% confidence upper limit on binary neutron star mergers of 1.26×10^4 yr^{-1}Gpc^{-3} (The LIGO Scientific Collaboration et al. 2016). With these assumptions, we would expect to find 1-2 KNe in our DES-SN sample. The second calculation is based on the hypothetical correspondence between KNe and short-hard gamma-ray bursts (SGRB, Paczynski 1986, Narayan et al. 1992). Assuming that the true event rate of SGRBs is the lower limit found in Fong et al. (2015) of 90 yr^{-1}Gpc^{-3} and that 1/2 of SGRBs are associated with KNe, the probability of seeing a KN in our sample is $\sim 4 \times 10^{-3}$.

We present results from the first untriggered optical search for KNe, which is complementary to the LIGO search for BNS mergers based on predicted GW signals. LIGO directly probes for mergers by looking for characteristic "chirp" GW signals from sources in its detection volume (The LIGO Scientific Collaboration et al. 2016). The DES KN search described here is sensitive to optical emission from such mergers. While we do not discuss optical follow-up to LIGO triggers, the methods and results presented here will inform strategies and contaminant rejection techniques for follow-up (Soares-Santos et al. 2016). The outline of this paper is as follows. In § 2 and § 3, we describe the DES data sample and the sim-

ulations, respectively. § 4 details selection requirements and our KN search efficiency for different models of host galaxy noise. The results and discussion of the analysis are presented in § 5 and § 6, and we conclude in § 7.

2. DES-SN DATA SAMPLE

For DES-SN, the CTIO Blanco-4m telescope and DECam were used to make repeated observations of ten 3 deg^2 fields. Each field was observed in *griz* bands with central wavelengths of 4830, 6430, 7830, 9180 Å, respectively. Eight of these fields were "shallow" fields with an average single-visit depth of $\sim$ 23.5 mag in each band. The other two were "deep" fields with an average single-visit depth of $\sim$ 24.5 mag in each band. The exposure time and number of exposures per visit are given in Table 1 of Kessler et al. (2015) (hereafter K15). The cadence was approximately one visit per week in each band and field. Transients were detected using the difference-imaging pipeline `DiffImg` described in K15 to find events with signal-to-noise ratio above 5 that also pass automated scanning to reject subtraction artifacts (Goldstein et al. 2015). To select candidates for SN science, DES-SN requires a detection on two separate nights, mainly to reject asteroids[1]. However, *all* candidates with two detections are saved, even if the two detections are on the same night.

For our KN search, we consider events with i and z detections close in time, since models predict that KNe will have higher SNR in the DES i and z bands than in g and r. Additionally, KNe are expected to fade on the timescale of repeat SN-field observations ($\sim$ 1 week). In the shallow fields, we require an i and z detection on the same night since all four (*griz*) bands are observed within $\sim$ 20 minutes anyway. In the deep fields, adjacent-night i and z detections are accepted since the four bands are not always observed on the same night. We define a *trigger* to be the first paired i and z detections of a candidate[2]. Longer time separations between i and z-band detections are not considered as triggers since KNe are expected to dim significantly between repeated observations of the fields.

Using the first two seasons of DES-SN, these criteria result in 3487 triggers in the shallow fields, and 1236 triggers in the deep fields, most of which are SNe and asteroids. Our data sample includes PSF-fitted measurements of the flux and its uncertainty in all four bands and all epochs, the angular separation between i and z-band detections on the trigger night (for asteroid rejection), the matched host galaxy, and its photometric redshift. The absolute photometric calibration of the sample has been validated at the 2% level (K15).

3. SIMULATIONS OF DES LIGHT CURVES

Monte Carlo simulations of KN and SN light curves, using the `SNANA` software package (Kessler et al. 2009), are employed to tune selection criteria, to determine the KN search efficiency, and to predict backgrounds. For an arbitrary light curve model, the `SNANA` simulation uses the observing conditions (PSF, zero point, sky noise) at each DES-SN epoch and passband to generate a redshifted[3] flux and uncertainty that would have been measured by `DiffImg`. The `SNANA` simulation generates light curves at the catalog-level and does not use images. As described in section 7 of K15, `SNANA` also does not fully account for image subtraction artifacts on bright galaxies. To better characterize the KN efficiency, we perform an additional study of fake point sources overlaid on the search images near low-redshift galaxies and processed with `DiffImg`.

KILONOVAE: We simulate KN light curves using rest-frame SED models from BK13. Their models have evolved since the start of this analysis (Barnes et al. 2016), but here we restrict ourselves to the original light curves of Barnes and Kasen (2013). The BK13 models are parameterized by the velocity $\beta = v/c$ and mass M of the matter ejected from the merger. BK13 generate nine SEDs corresponding to $\beta = [0.1, 0.2, 0.3]$ and $M = [0.001, 0.01, 0.1]\ M_\odot$, which we use in our analysis. Calculated *griz* light curves for all nine models are shown in Fig 1. These light curves are generically brightest in the z band, with decreasing brightness in bluer filters. At the time of maximum z-flux, the ratio of g, r, and i-band flux to z-band flux is 0.04, 0.2, and 0.5, respectively, when averaged over all nine models. Notably, the rest-frame brightness of these models spans 4-5 magnitudes, and the distribution over model parameters is unknown, adding to the uncertainty in overall KN detectability. In the `SNANA` simulation, KN light curve start times are randomly generated during the first season (Y1: 56534 $<$ MJD $<$ 56698) and second season (Y2: 56877 $<$ MJD $<$ 57067), and the redshift distribution is assumed to follow a constant co-moving volumetric rate. Our analysis considers KN light curves with and without host galaxy flux. When including host galaxy flux, the light curves are generated in the simulation such that the KN rate at a particular location is proportional to the background host brightness as described in § 4.4. To compute our sensitivity over a wide range of KN brightness, absolute magnitude offsets are applied as described in § 4 and § 5.

SUPERNOVAE: We perform simulations of Type Ia SNe using the SALT-II light curve model (Guy et al. 2010), the volumetric rate vs. redshift from Dilday et al. (2008), and the 'G10' intrinsic scatter model and the stretch and color populations from Kessler et al. (2013). For core collapse (CC) SNe we use CC templates as described in Kessler et al. (2010) and the rates from Li et al. (2011). Example i and z-band light curves simulated for a typical KN and SNIa are shown in Fig. 2. In general, the SNe tend to be bluer and have longer timescales than KNe. SN times of peak flux are simulated in the ranges MJD = 56450 to 56740 for Y1 and MJD = 56840 to 57110 for Y2. Each window extends $\sim$ 2 months before the start of the observing season, and $\sim$ 1 month after the end. These extended time windows account for long rise and fall times of SN light curves as well as the $(1 + z)$ time dilation for higher redshift SNe. SNe are generated in the redshift range $z < 1.35$. The probability of matching to a host galaxy is taken from Bernstein et al. (2012)[4]. Note

[1] See sections 3.2.4 and 3.3 in K15 for more details about science candidates

[2] Pairing requires that the RA and DEC of the i and z detections are within 1", and thus the angular (radial) separation extends out to $\sim \sqrt{2} \times 1$".

[3] The `SNANA` simulations use a FLRW cosmology with $H_0 =$ 70km/s/Mpc, $\Omega_M = 0.3$, and $\Omega_\Lambda = 0.7$.

[4] See $m_i < 24$ and $\kappa_{Ia} = 0.5$ column of Table 18.

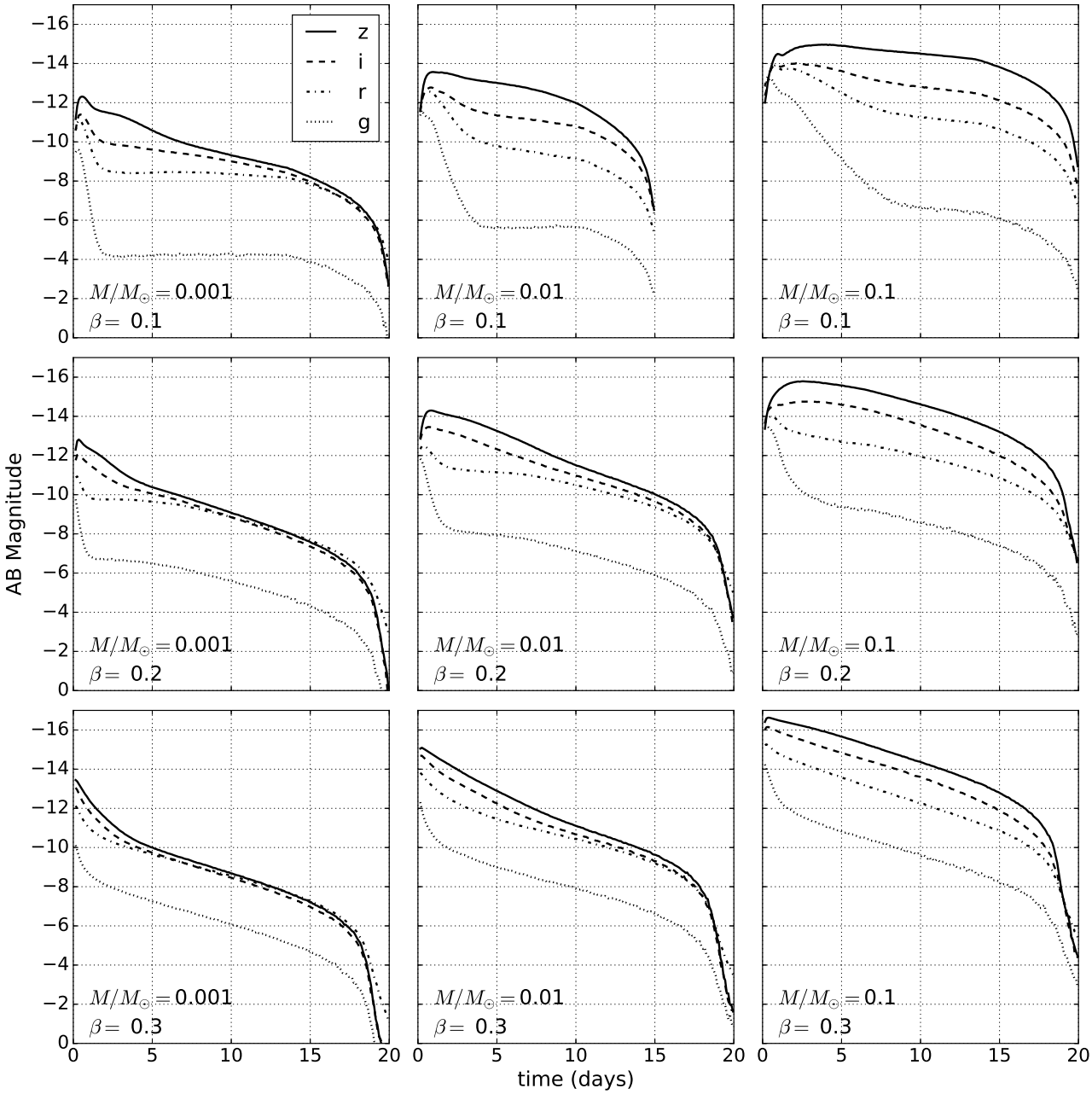

Figure 1. Computed *griz* broadband light curves from integrating the nine BK13 spectral energy distributions. The bottom left of each panel shows the BK13 model parameters.

that the simulation does not account for SNe matched to incorrect hosts. For each simulated host galaxy, the associated photometric redshift ($z_{\rm phot}$) is based on the photometric redshift distribution in the Science Verification (SV) catalogue described in Bonnett et al. (2015). To make SN background estimates with high statistical precision, we generate 3.7×10^5 SNIa and 4.3×10^6 CC SNe; this corresponds to 40 of our DES-SN data sets.

FAKES ON NEARBY GALAXIES: Following K15, we place fake point sources ("fakes") of random magnitudes onto CCD images to determine the efficiency of `DiffImg` in identifying sources on low-redshift galaxies. While the `SNANA` simulation accounts for increased noise from bright galaxies, processing fakes with `DiffImg` includes unmodeled inefficiencies that are not characterized by our simulation. As described in K15, there exists a "surface brightness anomaly" which degrades the `DiffImg` search efficiency for events on nearby galaxies. Pan-STARRS1 has also seen a similar anomaly (see Fig. 6 in Rest et al. 2014). To determine the effects of this anomaly on our search, we compute and compare the detection efficiencies from the `SNANA` and `DiffImg`+fakes methods for a range of source magnitudes and background surface brightnesses ($m_{\rm SB}$), where $m_{\rm SB}$ is the magnitude per square arcsecond measured on the template image. These two methods are used to independently quantify the results of our KN search, which we present in § 5. Since our analysis relies on i and z-band detections, the product of the i and z-band efficiencies gives the trigger

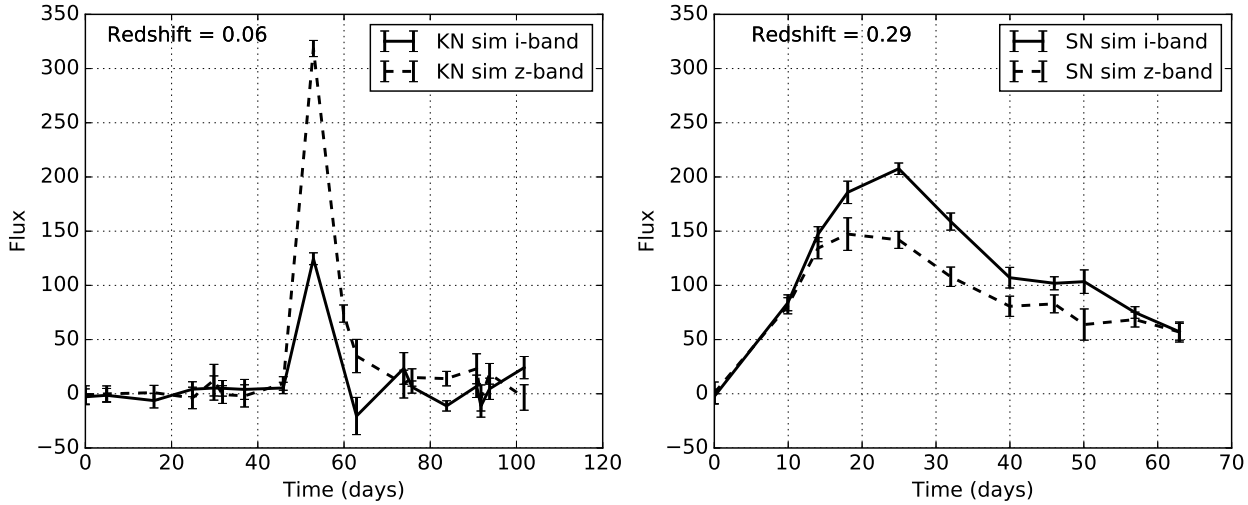

Figure 2. Observed KN and SN light curves in the i and z filters, as simulated with SNANA. The KN is based on the BK13 model with $\beta = 0.3$, $M = 0.1M_{\odot}$ and redshift $z = 0.06$. The SNIa is simulated with SALT-II color $c = 0.03$, stretch parameter $x_1 = -0.75$, and redshift $z = 0.29$. Magnitudes are given by $27.5 - 2.5\log_{10}(\text{Flux})$; e.g., the shallow-field detection limit of mag=23.5 corresponds to Flux=40. The error bars show the simulated flux and uncertainties for each observation; the lines connect these simulated points to guide the eye.

efficiency. Due to limited resources and a small number of low-redshift galaxies (~ 100) in the SN fields, we only test fake foreground magnitudes from 21st to 25th magnitude, and we do not run the difference imaging pipeline on fake BK13 light curves themselves.

NOT SIMULATED: Cowperthwaite and Berger (2015) (hereafter CB15) identify a number of objects other than SNe that could be KNe contaminants. These backgrounds are not simulated due to their low expected observation rate and are mostly removed with an $i-z$ color cut (see Fig. 3 in CB15). CB15 also found background objects with redder $i-z$ colors that could be consistent with the KN color: the Pan-STARRS fast transient PS1-13ess with $i-z = 0.62$ mag (Drout et al. 2014) and Type ".Ia" SNe (Shen et al. 2010). Tables 1 and 2 in CB15 show that the observation rate of these contaminants is about two orders of magnitude lower than the SN Ia observation rate, but still enough to contaminate KN signals. Nevertheless, these objects fail our selection requirements as described in § 4.2.

4. ANALYSIS

Our analysis extracts volumetric rest-frame rate limits from the DES-SN data sample using estimates of search time-volume and search efficiency. Following Dilday et al. (2008) (hereafter D08), the average KN rest-frame volumetric rate we infer is given by

$$R = N_{\rm KN}/[\widetilde{\epsilon_{\rm KN} VT}], \qquad (1)$$

where $\widetilde{\epsilon_{\rm KN} VT}$ is the effective time-volume probed by the survey for a volume V, observation time T, and efficiency as a function of redshift $\epsilon_{\rm KN}(z)$. $\widetilde{\epsilon_{\rm KN} VT}$ is computed from D08:

$$\widetilde{\epsilon_{\rm KN} VT} = (\Theta T)\int_{z_{min}}^{z_{max}} dz \epsilon(z) u^2(z) \frac{du}{dz}\frac{1}{(1+z)} \qquad (2)$$

Here, Θ is the solid angle probed by the survey in all fields and u is the FLRW metric comoving distance. The KN efficiency $\epsilon(z)$ is defined as the fraction of simulated KNe at redshift z passing the selection requirements described in § 4.1. Dependence of $\epsilon(z)$ on factors such as cadence and observing conditions are integrated out over the two DES seasons. We do not consider local density perturbations, which could affect volumetric rate estimates at low redshifts.

4.1. *Selection Requirements*

Here we describe the selection requirements (cuts) applied to the data and simulated events. The cuts were designed to exclude SNe while maximizing KN efficiency.

1. A *KN trigger* requires paired i- and z-band detections, where a detection is described in K15. Both detections pass automated image scanning described in Goldstein et al. (2015). We also require that both detections have a signal-to-noise ratio (SNR) greater than 5. The i- and z-band detections must occur on the same night for a KN trigger except in the deep fields where adjacent night detections are allowed due to longer deep-field exposure times. A candidate can only KN trigger once: the first paired $i+z$ detection of a candidate is taken as the KN trigger and subsequent $i+z$ detections of the same candidate are not considered additional triggers.

2. For each i- and z-band detection in cut 1, we require zero point (ZP) $>$ ZP$_{\rm median}-0.2$ mag: ZP$_{\rm median}$ is the median of the ZP distribution for KN trigger i and z detections, and it is calculated independently for the shallow and deep fields. This cut ensures reasonable atmospheric transparency during the KN trigger observations.

3. For each i- and z-band detection in cut 1, we require PSF full width at half maximum < 2.0 arcsec.

4. The ratio g-flux/z-flux < 0.15 on the KN trigger night. If the i and z bands are observed on adjacent nights (in the deep fields), the g-band flux on the earliest night of the KN trigger is used. Considering

all nine BK13 models, the g-flux is at most 0.09 times the z-flux at time of peak z-flux. The cut is well above the maximum g-flux/z-flux to accept events with reasonably large Poisson fluctuations.

5. r-flux/z-flux < 0.4: Similar to the g-flux/z-flux cut except using the r band rather than the g band. Considering all nine BK13 models, the r-flux is at most 0.37 times the z-flux at time of peak z-flux.

6. There is at least one i or z band observation (regardless of SNR) 3 to 10 days[5] after the KN trigger: This ensures sufficient data to examine the light curve evolution.

7. There is at least one observation (independent of SNR) 2 to 14 days before the trigger: ensures the ability to identify (and reject) light curves that begin before the trigger.

8. There is at least one observation (independent of SNR) 20 to 100 days after the trigger: ensures the ability to identify (and reject) light curves that continue after any KN would have faded.

9. There is no SNR > 4 observation 2 to 14 days before the trigger: rejects objects that are bright before the KN trigger.

10. There is no SNR > 4 observation more than 20 days after the trigger: We define the time difference between the last single-band detection and the KN trigger $\Delta t \equiv t_{\rm last} - t_{\rm trigger}$ and require $\Delta t < 20$ days to reject objects with long timescales.

11. Veto events matched to a host galaxy with $z_{\rm phot} > 0.3$: Since we are sensitive to KNe at low redshift ($z < 0.3$), we remove events associated with a high redshift galaxy. The requirement for matching a source to a host galaxy is a source-host galaxy angular separation $< 2''$ and a directional light radius separation of $d_{LR} < 2$ (Sako et al. 2014; Gupta et al. 2016). This matching requirement is more strict than the K15 requirement of $d_{LR} < 4$, and was adjusted to avoid too many false matches to hosts, which lowers the KN efficiency. If a source is matched to a host, it is vetoed if the host has $z_{\rm phot} > 0.3$. Given the DES-SN limiting magnitudes, transients detected with $z_{\rm phot} > 0.3$ have peak absolute magnitude brighter than ~ -16.5 mag in the deep fields and -17.5 mag in the shallow. Note that transients with no detected host galaxy will have no $z_{\rm phot}$ and thus this veto will not apply.

12. shape < 0. Here we define the 'shape' as the rate of change of the z-band flux (normalized to the KN trigger z-band flux) between the night of the KN trigger and the next z-band observation:

$$\text{shape} = \frac{1}{F_1}\frac{F_2 - F_1}{t_2 - t_1}, \quad (3)$$

where F_1 and t_1 are the z-band flux and MJD of the KN trigger, respectively. F_2 and t_2 are the flux and MJD of the next z-band observation after the KN trigger, respectively. This shape cut removes events that do not exhibit a declining light curve after the trigger.

[5] All temporal cuts are made in the observer frame.

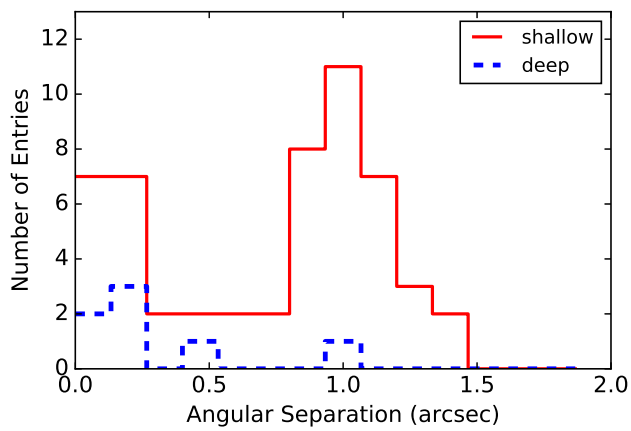

Figure 3. Distributions of the angular separation between KN trigger i and z observations δ_{iz} for the DES-SN data. The first ten cuts are applied. A few objects with outlying δ_{iz} are not shown on the plot.

13. *angular separation* (δ_{iz}) between the KN trigger i and z observations of the transient < 0.6": This cut removes contamination from asteroids. The δ_{iz} distribution is shown in Fig. 3 for the deep and shallow fields after applying the first 10 cuts. The deep field exposure times for the i and z bands are 1800 and 3600 seconds respectively, long enough that moving asteroids fail the PSF-shape requirement. The deep field sample is thus dominated by non-moving transients, and the δ_{iz} distribution is peaked near 0.1", consistent with the astrometric precision. The shallow field exposure times are much shorter, 200 and 400 seconds for i and z band respectively, and thus slow-moving asteroids are included by the 1" trigger-matching requirement in `DiffImg`. Fig. 3 shows that the shallow field δ_{iz} distribution has two components: 1) a non-moving component at $\delta_{iz} \sim 0.1$ and 2) a moving component with more events as δ_{iz} increases.

    Further evidence for asteroid contamination is the excess of events in the four shallow fields near the ecliptic where most asteroids orbit. After applying the first 10 cuts, there are a total of 42 events in these four fields, while the four shallow fields away from the ecliptic have a total of 11 remaining events. In contrast, the two deep fields (one near the ecliptic and one away from the ecliptic) each contain the same number of events (4) after cut 10, showing that the deep fields are less susceptible to asteroid contamination.

14. KN trigger $i - z$ color > 0.5 mag: Motivated by the BK13 predictions that KNe are very red, we require $i - z > 0.5$ for the trigger bands.

We exclude one cut at a time from the analysis to determine the effectiveness of each cut. We find that the four cuts which maximally suppress SN background, in order of effectiveness, are cuts 9, 14, 10, and 11. Though

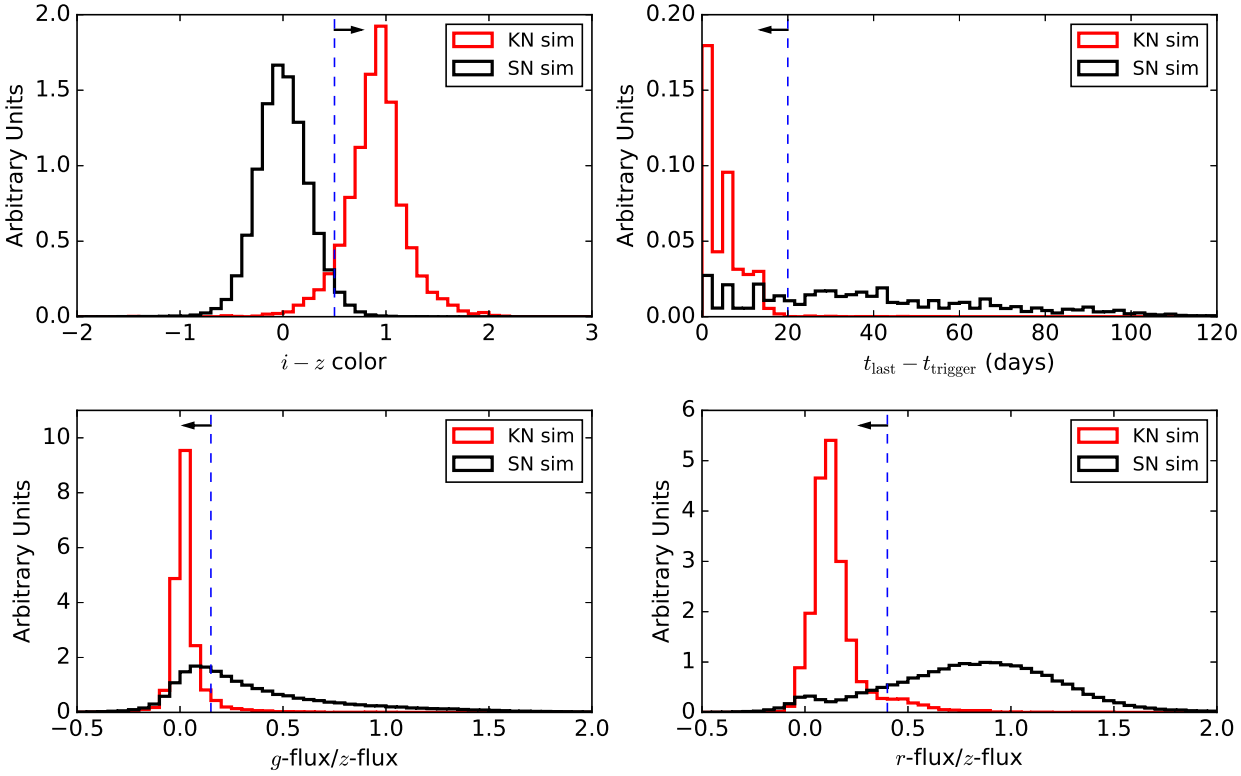

Figure 4. Simulated distributions of KN and SN triggers (cut 1). The dashed vertical lines show the values of the cuts, and the arrows show the selected sample. *Top left panel:* $i-z$ colors. *Top right:* Time between first trigger and last single-band detection. *Bottom left:* ratio of g-flux to z-flux for a trigger. Negative values are allowed, since negative fluxes can occur due to forced photometry. *Bottom right:* ratio of r-flux to z-flux for a trigger.

Table 1
Number of Events and Simulated Efficiencies for each Selection Requirement

	Shallow Fields					Deep Fields				
Cuts	Data	sim SN[a]	eff$_{\rm CC}$[b]	eff$_{\rm Ia}$[b]	eff$_{\rm KN}$[bc]	Data	sim SN[a]	eff$_{\rm CC}$[b]	eff$_{\rm Ia}$[b]	eff$_{\rm KN}$[bc]
1. i+z trigger	3487	1214	0.01	0.28	4.3	1236	1062	0.045	0.89	3.9
2. ZP $<$ ZP$_{\rm median}$	3300	1172	0.01	0.27	4.1	1180	1010	0.043	0.85	3.7
3. trigger PSF(i,z) $<$ 2.0 ”	3074	1139	0.0098	0.27	3.9	1176	1004	0.042	0.84	3.6
4. gflux/zflux $<$ 0.15	550	237	0.0019	0.057	3.7	407	562	0.019	0.53	3.4
5. rflux/zflux $<$ 0.4	209	34	0.0005	0.0058	3.6	213	280	0.009	0.27	3.3
6. observed 3-10 days after trigger	195	28	0.0004	0.0045	3.1	169	214	0.0069	0.21	2.9
7. observed 2-14 days before trigger	172	22	0.0003	0.0033	3	152	189	0.0061	0.18	2.8
8. observed 20 to 100 days after trigger	164	20	0.0003	0.0032	2.6	148	175	0.0055	0.17	2.7
9. no SNR $>$ 4 observed 2 to 14 days before trigger	61	5.1	8×10^{-5}	0.0008	2.6	24[d]	42	0.0014	0.041	2.5
10. no SNR $>$ 4 observed 20 days after trigger	53	4.0	6×10^{-5}	0.0007	2.5	8	11	0.0004	0.0096	2.5
11. veto z_{phot} $>$0.3	51	1.9	3×10^{-5}	0.0004	2.3	2	6.2	0.0002	0.0058	2.2
12. shape $<$ 0.0	47	1.4	2×10^{-5}	0.0002	2.2	2	3.9	0.0001	0.0035	2.2
13. $\delta_{iz}<$ 0.6 arcsec	12	1.4	2×10^{-5}	0.0002	2.2	1	3.9	0.0001	0.0035	2.2
14. i-z color $>$ 0.5	0	0.17	3×10^{-6}	2×10^{-5}	2.2	0	0.96	3×10^{-5}	0.0009	2.1

[a]Since 40 SN data sets are simulated for better statistics, the numbers of simulated SN events are divided by 40 to correspond to one DES-SN data set. The statistical uncertainty in each sim SN line is $\sqrt{N_{\rm SN}/40}$, where $N_{\rm SN}$ is the number of simulated events on a given line.

[b]eff$_{\rm CC}$, eff$_{\rm Ia}$, and eff$_{\rm KN}$ are the simulated efficiencies of CC SNe, SNIa, and KNe, respectively. They are quoted in percent.

[c]Based on a random assortment of BK13 light curves generated randomly in co-moving volume out to redshift 0.15 in shallow fields and 0.2 in deep fields assuming no host galaxy noise. The KN efficiencies shown here are small due to the large redshift range of the simulation.

[d]The 2.8σ difference between the SN simulation prediction and data here is not unexpected: We estimate a $\sim$ 30% chance of there being such a deviation in the table by performing a Monte Carlo simulation of data values in the table given the numbers from the SN simulation.

the g- and r-band cuts (4 and 5) are not among the most effective cuts for SNe, we still require these color cuts to reject other backgrounds, as described in § 4.2. The simulated distributions of the three colors (cuts 4, 5, and 14) and Δt (cut 10) are shown in Fig. 4 for KNe and SNe. The KN distributions shown here are based on a random assortment of the nine BK13 models placed uniformly in co-moving volume out to $z = 0.15$ in the shallow fields and $z = 0.2$ in the deep fields.

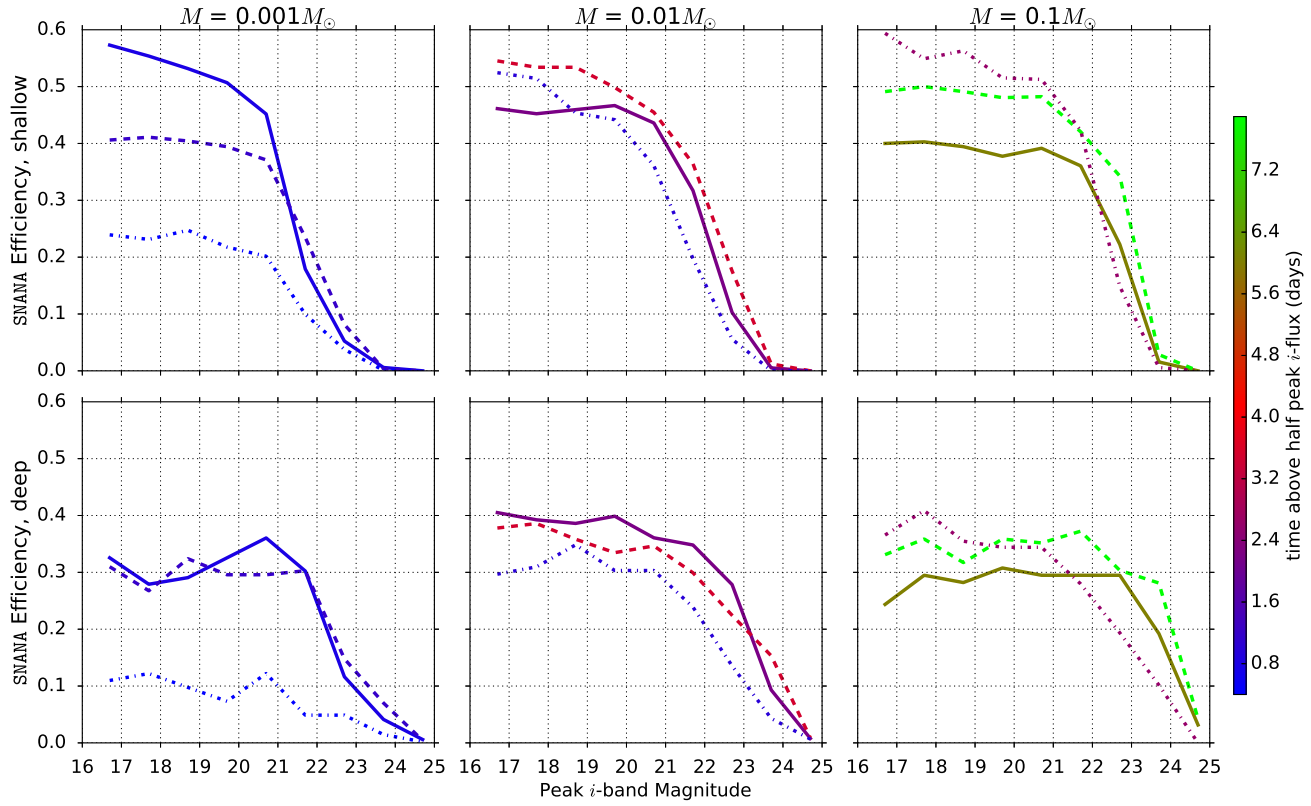

Figure 5. KN search efficiency as a function of peak apparent i-band magnitude for the BK13 models in the shallow and deep fields at fiducial redshift $z = 0.02$. Efficiencies do not account for host galaxy noise. The solid, dashed, and dashed-dotted lines correspond to BK13 models with $\beta = 0.1, 0.2, 0.3$, respectively. The colors of the lines represent each model's $t_{\rm half}$, the time above half maximum flux in the i-band.

Table 2
KN efficiency for peak $m_i = 18$[a]

	KN efficiency for		
Cut	$\beta = 0.1$	$\beta = 0.2$	$\beta = 0.3$
1. i+z trigger	0.99	0.99	0.99
2. ZP $<$ ZP$_{\rm median}$	0.88	0.90	0.88
3. trigger PSF(i,z) $<$ 2.0 arcsec	0.77	0.77	0.78
4. gflux/zflux $<$ 0.15	0.64	0.72	0.78
5. rflux/zflux $<$ 0.4	0.59	0.72	0.78
6. observed 3 to 10 days after trigger	0.55	0.69	0.73
7. observed 2 to 14 days before trigger	0.53	0.66	0.71
8. observed 20 to 100 days after trigger	0.47	0.60	0.64
9. no SNR $>$ 4 observed 2 to 14 days before trigger	0.45	0.58	0.63
10. no SNR $>$ 4 observed $>$ 20 days after trigger	0.44	0.58	0.62
11. veto z_{phot} $>$0.3	0.41	0.53	0.55
12. shape $<$ 0.0	0.40	0.50	0.55
13. $\delta_{iz}$$<$ 0.6 arcsec	0.40	0.50	0.55
14. i-z color $>$ 0.5 mag	0.40	0.50	0.55

[a]BK13 $M = 0.1M_\odot$ models simulated in shallow fields with `SNANA`, where each model is scaled to have peak i band magnitude $m_i = 18$.

The number of data and simulated events remaining after each cut is shown in Table 1. No events from the DES-SN sample pass all of our cuts, and the SN simulation predicts 1.1 ± 0.2 total background events.

4.2. *Efficiency for Transients that are Not Simulated*

The cuts are tuned solely on the SN simulations but are effective at removing other backgrounds as well. As mentioned in §3, Type ".Ia" SNe and Pan-STARRS fast transients like PS1-13ess have $i-z$ colors consistent with KNe. PS1-13ess is bright in the g-band relative to the z-band (Drout et al. 2014), so objects like it are rejected with a cut on the g brightness (cut 4). ".Ia" models from Shen et al. (2010) produce spectra that are initially a blue continuum, but redden at late times as the model dims. Such light curves are removed with cuts 4, 5, and 9, which remove events with bright r or g-band flux before or during the KN trigger.

4.3. *KN efficiency with no host galaxy*

To calculate KN rates using Equations 1 and 2, the KN efficiency as a function of redshift or apparent magnitude is required. Fig. 5 shows the efficiency versus peak apparent magnitude for the nine BK13 models. To generate these curves, we vary the absolute magnitude of BK13 light curves and simulate them at a fiducial redshift of $z = 0.02$ with no host galaxy noise. Here, a fiducial redshift is used so that the dependence of efficiency on observed brightness can be compared between models, while being agnostic to each model's absolute magnitude.

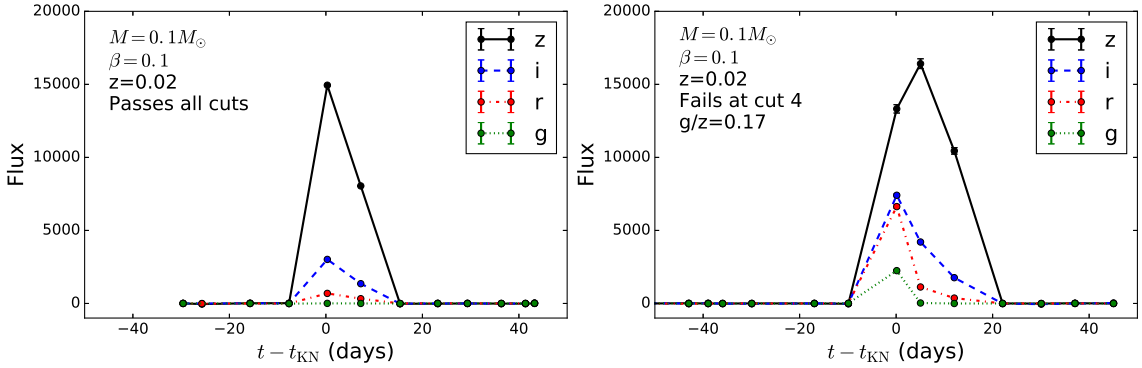

Figure 6. Example *griz* $\beta = 0.1$, $M = 0.1 M_\odot$ light curves at magnitude 18 that pass the cuts (left) and fail the cuts at cut 4 (right). The points show the observed fluxes and lines are drawn between them to guide the eye. Fluxes are defined such that magnitudes are given by $27.5 - 2.5 \log_{10}(\text{Flux})$; e.g., mag=22.5 for Flux=100.

Our final rate calculations, however, use analogous efficiency curves and include redshifting based on absolute magnitudes from BK13. At bright apparent magnitudes, the efficiencies do not reach unity due to the DES-SN cadence and selection requirements.

To further illustrate selection effects, Fig. 5 shows the timescale of each KN model, parameterized by the time above half maximum flux in the i band $t_{\rm half}$. Near the detection limit (mag 23.5 for shallow fields, mag 24.5 for deep), KNe with longer $t_{\rm half}$ are more detectable, because there are more chances to make a detection than for short-$t_{\rm half}$ KNe. However, this relation between efficiency and $t_{\rm half}$ does not hold at magnitudes much brighter than the detection limit. For a bright KN, there are multiple chances to detect the light curve before it falls below the detection threshold, so the selection requirements rather than $t_{\rm half}$ drive the efficiency for each model.

For comparison between models, Table 2 shows the efficiency of each $M = 0.1 M_\odot$ model at magnitude 18 (~ 5 mag brighter than threshold) and $z = 0.02$ in the shallow fields with each cut. The cut on the ratio of g-flux to z-flux (cut 4) significantly reduces the $\beta = 0.1$, $M = 0.1 M_\odot$ efficiency, showing how the interplay between color and cuts will affect the efficiency of bright sources. Example 18th magnitude $\beta = 0.1$, $M = 0.1 M_\odot$ light curves are shown in Fig. 6.

4.4. *KN efficiency with underlying host galaxy*

Here we investigate two anomalous effects from difference imaging on bright galaxies that result in efficiency losses: 1) excess missed detections of point sources, and 2) excess flux scatter which affects analysis selection requirement efficiency. For the first effect, poor subtractions can result in KN events that are not detected or that result in detections which look like missubtractions and thus fail the automated scanning. To investigate the detection efficiency losses, we use fakes to measure single-band, single-epoch *detection* efficiencies for `DiffImg` ($\epsilon_{\texttt{DiffImg}}$[6]) as a function of background surface brightness ($m_{\rm SB}$). The single-epoch efficiency in the `SNANA` simulation ($\epsilon_{\texttt{SNANA}}$) accounts for host galaxy Poisson noise as well as excess flux scatter from the SB anomaly, but does not account for detection losses. We therefore use the `DiffImg` detection efficiencies, measured with fake sources on galaxies, to correct $\epsilon_{\texttt{SNANA}}$.

The second image-subtraction effect is from detected KNe with excess flux scatter. We characterize the impact on the analysis efficiency by including this excess scatter in the simulation (see Figs. 9-10 in K15). In this analysis, we do not consider the effect of correlations between measured fluxes in different bands and correlations between fluxes and detections. Additionally, our analysis does not account for the effects of image subtraction artifacts on δ_{iz}.

To characterize the detection efficiencies with and without a host galaxy, and to compare `SNANA` and `DiffImg`, we define an efficiency ratio,

$$\mathcal{R}_\epsilon \equiv \epsilon / \epsilon_{\rm NoHost,\texttt{SNANA}} \tag{4}$$

where ϵ is the detection efficiency of either `SNANA` or `DiffImg` and $\epsilon_{\rm NoHost,\texttt{SNANA}}$ is the `SNANA` efficiency with no host galaxy. Since $\epsilon_{\rm NoHost,\texttt{SNANA}}$ is the highest possible efficiency, we expect $\mathcal{R}_\epsilon \leq 1$, except for statistical fluctuations. Fig. 7 shows the ratio $\mathcal{R}_\epsilon$ for the i-band shallow fields, where ϵ is 1) $\epsilon_{\texttt{SNANA}}$, 2) $\epsilon_{\rm NoHost,\texttt{DiffImg}}$, and 3) $\epsilon_{\texttt{DiffImg}}$. To compute our KN search sensitivity, we have similar information for the z-band and the deep fields.

The simulation of $\epsilon_{\texttt{SNANA}}$ shown in Fig. 7 demonstrates that host Poisson noise has almost no effect on the detection efficiency for source magnitude $m_i = 21 - 22$ mag. However, near the detection limit ($m_i = 23 - 24$ mag), $\epsilon_{\texttt{SNANA}}$ falls to half the no-host efficiency when the surface brightness reaches $m_{\rm SB} \sim 19$ mag/asec^2, which is comparable to sky noise of 19.6 mag/asec^2. The efficiency loss from host Poisson noise can not be mitigated, and represents the upper limit on the efficiency from `DiffImg`.

Fig. 7 also shows that the `DiffImg` efficiency with no host galaxy noise $\epsilon_{\rm NoHost,\texttt{DiffImg}}$ agrees with the no-host efficiencies predicted using `SNANA` ($\epsilon_{\rm NoHost,\texttt{SNANA}}$). For $m_{\rm SB} \gtrsim 26$, $\epsilon_{\texttt{SNANA}}$ and $\epsilon_{\texttt{DiffImg}}$ converge to $\epsilon_{\rm NoHost,\texttt{SNANA}}$, demonstrating that very faint backgrounds do not degrade efficiency. For brighter backgrounds, the `DiffImg` efficiency ($\epsilon_{\texttt{DiffImg}}$) deviates from the `SNANA` efficiency ($\epsilon_{\texttt{SNANA}}$) that simulates Poisson noise. At a given surface brightness, $\epsilon_{\texttt{DiffImg}}$ is lower than $\epsilon_{\texttt{SNANA}}$, because of the SB anomaly described in K15[7]. For large background

[6] ϵ includes the host galaxy noise unless a "noHost" subscript is included

[7] Note that K15 characterized excess scatter in the measured flux, not degraded efficiency: since there are many opportunities to detect the light curve of a bright SNIa, SNIa detection efficiency is not affected by the SB anomaly.

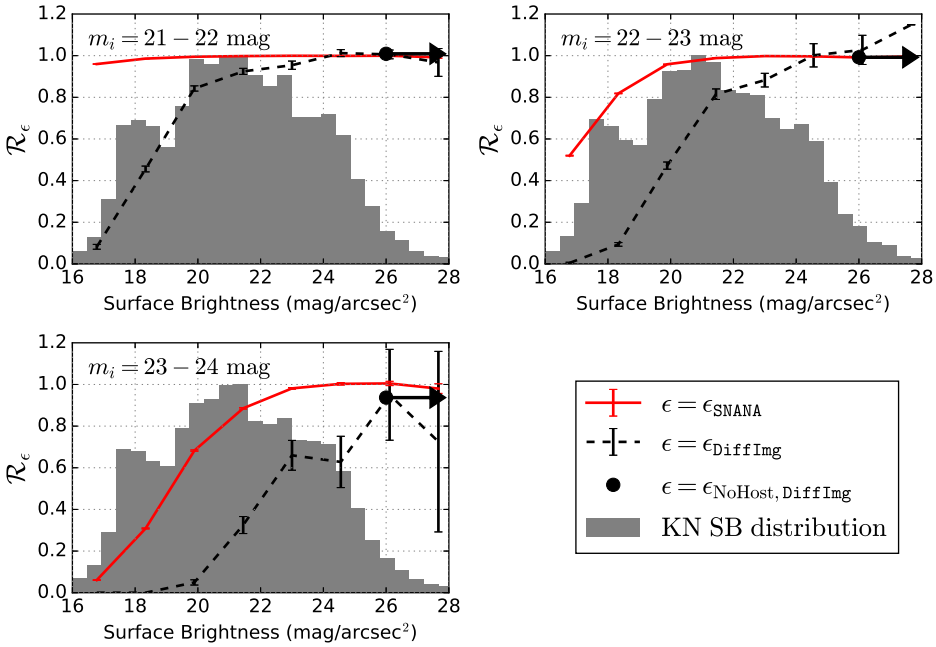

Figure 7. $\mathcal{R}_\epsilon$ in the DES-SN shallow fields vs. $m_{\rm SB}$ for KN i-band magnitudes (a) m_i = 21-22, (b) 22-23, and (c) 23-24. The solid red line is based on the `SNANA` simulation, and the dashed black line is from fake point sources processed by `DiffImg`. The gray regions show the i-band surface brightness distribution in the shallow-field, calculated in `SNANA` from the DES+2MASS catalogue Sersic profiles. The black dot and arrow shows $\mathcal{R}_\epsilon$ for `DiffImg` fakes with $m_{\rm SB} > 26$, i.e. with no host galaxy. The error bars show 1σ uncertainties.

brightnesses, the SB anomaly has a significant effect on the efficiency. For fakes with 21 mag $< m_i <$ 22 mag and 17 mag $< m_{\rm SB} <$ 18 mag/asec^2, $\sim$ 60% are detected on the subtracted image, but only 2% of these pass automated image scanning because of poor quality subtractions. An example search and difference image for an undetected fake on a bright galaxy is shown in Fig. 8. This particular fake has an i-band magnitude of 21.2 mag and $m_{\rm SB}$ = 17.6 mag/asec^2. The subtracted image shows a dipole structure and fails the automated scanning.

To estimate the total search sensitivity degradation from host galaxy noise, the efficiency is weighted by the KN distribution of background surface brightness $m_{\rm SB}$[8]. This distribution has not been predicted, so here we generate KNe at surface brightnesses following the Sersic profiles of the "DES+2MASS" and SV galaxy catalogues. This procedure assumes that the KN rate density follows the background surface brightness. The DES+2MASS catalogue includes galaxies from the 2MPZ catalogue within 200 Mpc (Bilicki et al. 2014). We use the following information from the galaxy catalogues: sky coordinates, redshift, i- and z-band magnitude, absolute magnitude, and shape profile. The gray-shaded region in Fig. 7 shows the i-band surface brightness distribution for KNe derived from the DES+2MASS+SV galaxy catalogue Sersic fits assuming the KN volumetric rate follows galaxy profiles. While the $m_{\rm SB}$ distribution depends on the choice of galaxy catalog and model assumptions, the efficiency curves are much less sensitive to these choices. Additionally, we have not investigated potential δ_{iz} artifacts from image subtractions.

[8] Uncertainties on efficiency are shown in Fig. 7 for illustrative purposes, but are not propagated through the analysis since host galaxy model uncertainties dominate.

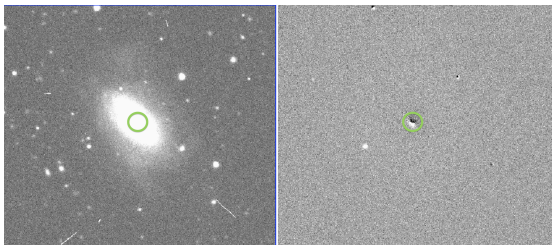

Figure 8. Search (left) and difference (right) images for an undetected fake with source magnitude m_i = 21.2 mag and $m_{\rm SB}$ = 17.6 mag/asec^2. The fake is shown at the center of the green circle. Each image is 2.3'×2.3'.

We next compute the average $\epsilon_{\texttt{DiffImg}}/\epsilon_{\texttt{SNANA}}$ (ie. excess detection efficiency loss) as a function of KN magnitude weighted by the $m_{\rm SB}$ distribution. For $m_{\rm SB}$ below and above where $\epsilon_{\texttt{DiffImg}}$ is known, the efficiency ratio is set to 0 and $\texttt{max}(\epsilon_{\texttt{DiffImg}}/\epsilon_{\texttt{SNANA}})$, respectively. We then use `SNANA` to simulate analogous efficiency curves to those in Fig. 5, this time including host galaxy Poisson noise and SB-anomaly excess flux scatter. These new efficiency curves are then down-weighted by the excess detection efficiency loss to give the overall KN efficiency as a function of KN magnitude. Since the brightest fakes in the `DiffImg` test are m_i = 21 mag, we linearly extrapolate $\epsilon_{\texttt{DiffImg}}/\epsilon_{\texttt{SNANA}}$ to mag 16 where $\epsilon_{\texttt{DiffImg}}/\epsilon_{\texttt{SNANA}}$ is assumed to be 1. The recomputed efficiencies which account for the SB anomaly are used to calculate KN volumetric rates in § 5.

5. RESULTS

5.1. *Event selection and contamination*

The number of events passing each cut for the data, simulated KNe, and simulated Ia and CC SNe are shown in Table 1. For the simulations, efficiencies are shown as well. The KN efficiencies in Table 1 are based on a dif-

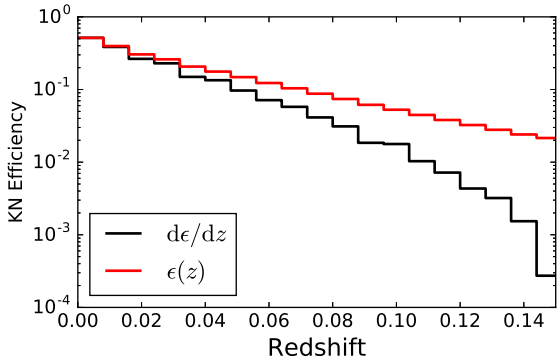

Figure 9. Efficiency per redshift bin $d\epsilon/dz$ and cumulative efficiency $\epsilon(z)$ in the shallow fields.

ferent simulation than the 18th magnitude KN efficiencies in Table 2. Table 1 shows the efficiencies for BK13 models simulated randomly in co-moving volume out to redshift 0.15 in the shallow fields and 0.2 in the deep fields with no host galaxies. In comparison to Table 2, the KN efficiency here is much lower (2%) because the simulated redshift range goes beyond the detectable distance of most BK13 models. Fig. 9 shows the efficiency per redshift bin ($d\epsilon/dz$) and cumulative efficiency (ϵ) as a function of redshift for this KN simulation in the shallow fields. The cumulative efficiency falls off as the redshift range is increased, showing that the redshift range and KN absolute magnitude are driving the overall efficiency shown in Table 1. At redshifts near 0, the efficiency plateaus at ~ 0.35 rather than 1 because 30% of the low-redshift KNe do not meet the KN trigger requirement, and there is added loss from the other selection requirements. At $z = 0.15$ the cumulative efficiency in Fig. 9 matches the KN efficiency shown in the shallow column of Table 1.

During the first two years of DES-SN, 3487 and 1236 KN triggers were identified in the shallow and deep fields, respectively. As mentioned earlier, asteroids contaminate the shallow fields, so the SN simulations under-predict the number of data triggers. The deep-field triggers however are well described by the SN simulations. Fig. 10 shows the distributions of host galaxy $z_{\rm phot}$ and $i - z$ color for the SN simulations (normalized to 2 seasons) and the data in the deep fields. The simulated distributions agree well with those from the data and show that the SN simulations predict the non-asteroid background levels. After all cuts, no events remain, which is consistent with our simulation prediction of 1.1 ± 0.2 SN events: 0.96 in the deep fields and 0.17 in the shallow fields. There is a 33% chance of finding 0 events in the sample given the SN prediction.

While no events pass our cuts in this search, SNe could contaminate future KN searches (e.g. Cowperthwaite et al. 2016). Fig. 11 shows example light curves for simulated CC and Ia which pass all the cuts. About 40% of the simulated SN background are CC, suggesting that Ia and CC SNe contribute similarly to the KN-search background. The Ia and CC contaminants have mean redshifts in the simulation of 1.1 and 0.8, respectively, but do not have measured $z_{\rm phot}$ values, and thus can not be vetoed by cut 11. Fig. 12 shows the Ia and CC efficiency as a function of simulated redshift. At low redshift, the SNe have low efficiency because they exhibit blue light curves and their light curves pass the detection threshold well past 20 days and thus fail the veto (cut 10). However, sufficiently redshifted SNe can take on the red colors of KN light curves and pass cuts 4, 5, and 14. These simulated contaminants illustrate that high-redshift SNe with no photometric redshift are the primary background for KN searches.

5.2. *Rate limits*

Here we calculate 90% upper rate limits using Equations 1 and 2, efficiencies from § 4, and two different assumptions: no host galaxy noise and host galaxy noise including the detection and selection-requirement efficiency loss from the SB anomaly. For these rate calculations, efficiencies differ from those presented in § 4, as redshift effects are included rather than simulating at the fixed redshift $z = 0.02$. The first assumption with no host galaxy corresponds to each BNS system being ejected from its host galaxy or occurring in a faint galaxy. For this assumption, we use $\epsilon_{\rm NoHost,\texttt{SNANA}}$ (Fig. 5) to calculate the rate limits. The red points in Fig. 13 show the upper rate limits for the nine BK13 models assuming all BNS systems are "kicked" out of galaxies. For the brightest model, the upper rate limit is 2.4×10^4 Gpc^{-3}yr^{-1}, while for the dimmest it is 1.0×10^7 Gpc^{-3}yr^{-1}. We also compute rate limits as a function of absolute magnitude for BK13 models, which are shown as black lines in Fig. 13.

Next we consider the second assumption where all BNS systems remain in the galaxy and are distributed based on background SB, whose distribution is that described in § 4.4. We use $\epsilon_{\texttt{DiffImg}}(z)$ rather than $\epsilon_{\rm NoHost,\texttt{SNANA}}(z)$ for detections and include the excess flux scatter effects in the selection-requirement efficiency. In this case, the limits are 5.2×10^4Gpc^{-3}yr^{-1} and 4.6×10^7 Gpc^{-3}yr^{-1} for the brightest and dimmest BK13 models, respectively. Fig. 14 is analogous to Fig. 13, but shows the rate limits for KNe in galaxies and includes detection and selection-requirement efficiency loss from Poisson noise and the SB anomaly. The rate limits on all nine models with and without host galaxy noise are given in Table 3. The KN rate upper limits with host galaxy noise are ~ 3 times higher than the upper limits for KNe with no detectable host. The SB anomaly is largely responsible for the decreased sensitivity: the rates calculated with just host Poisson noise are only 10% higher than with no host galaxy, showing the SB anomaly has a significant impact on the KN search.

Table 3
The 90% upper rate limits for the BK13 models

$M/M_\odot$	β	peak M_i	upper rate limit (Gpc^{-3}yr^{-1})	
			no host	+ host
0.001	0.1	−11.4	1.0×10^7	4.6×10^7
0.001	0.2	−12.0	4.0×10^6	1.5×10^7
0.001	0.3	−13.1	2.8×10^6	1.0×10^7
0.01	0.1	−12.8	1.1×10^6	3.3×10^6
0.01	0.2	−13.5	4.4×10^5	1.3×10^6
0.01	0.3	−14.7	2.1×10^5	5.7×10^5
0.1	0.1	−14.0	1.5×10^5	5.1×10^5
0.1	0.2	−14.8	7.0×10^4	2.1×10^5
0.1	0.3	−16.2	2.4×10^4	5.2×10^4

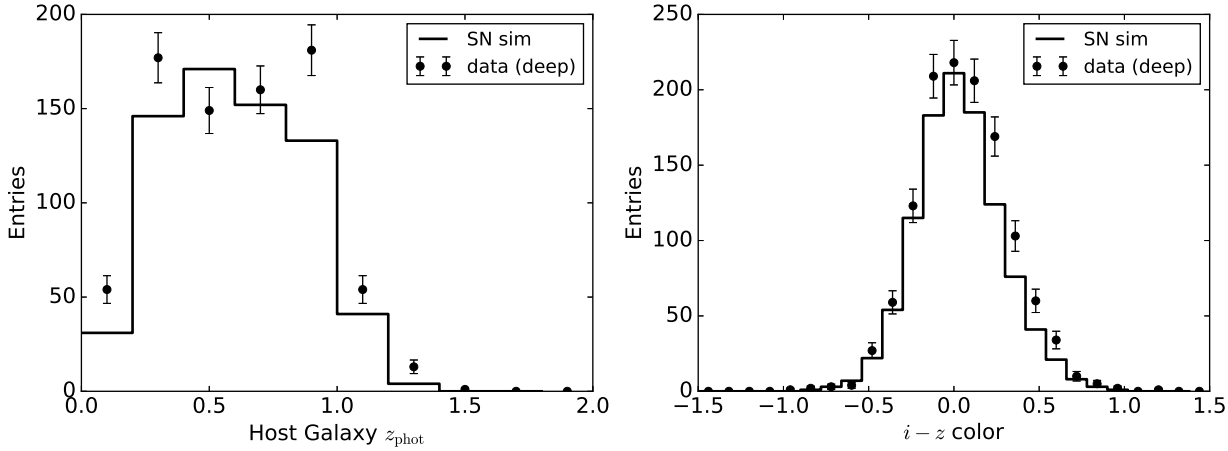

Figure 10. Left: for objects matched to a host galaxy, the distribution of deep field KN trigger $z_{\rm phot}$ is shown for the data (solid circles) and the SN simulation (histogram). Right: Distribution of KN trigger i-z color. The simulation has been re-scaled by 1/40 to correspond to two DES seasons.

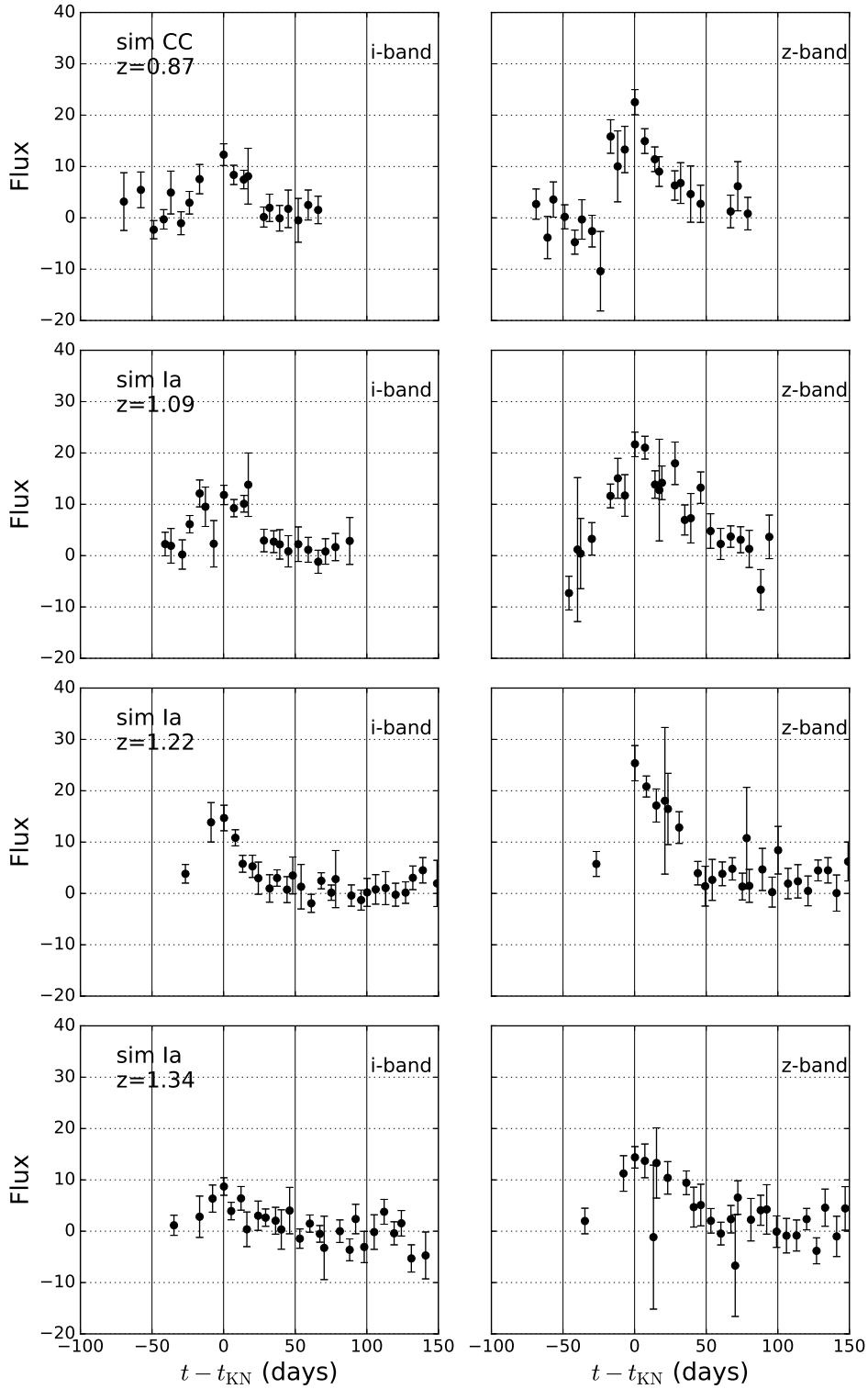

Figure 11. Example i and z-band light curves for simulated CC and Ia which passed all cuts. Fluxes are defined such that magnitudes are given by $27.5 - 2.5\log_{10}(\text{Flux})$; e.g., mag=25 for Flux=10.

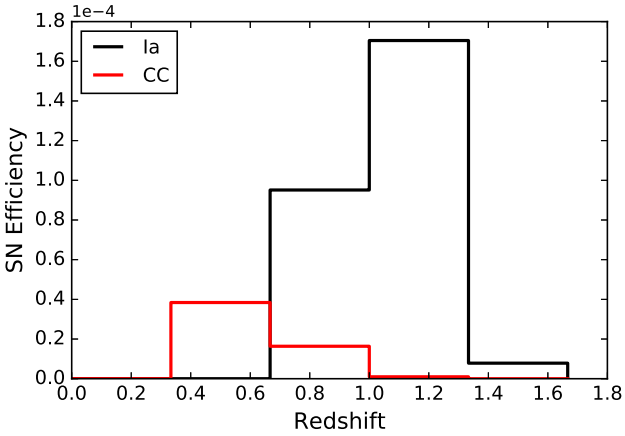

Figure 12. Simulated efficiency of Ia and CC SNe as a function of redshift. Note that the y-axis is scaled by 10^{-4}.

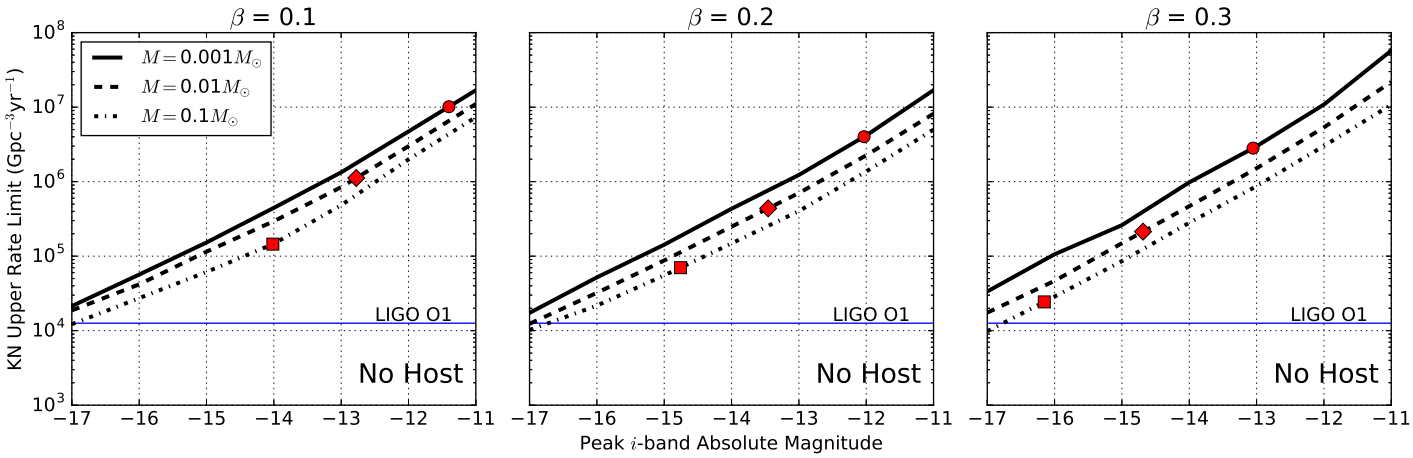

Figure 13. The 90% upper rate limit for the nine BK13 models using efficiencies calculated with `SNANA`. Each BK13 model is offset in absolute magnitude and the search efficiency is determined to calculate the rate. The red points show the rate limits for each model with no magnitude offset. The blue line shows the upper limit set in Advanced LIGO O1 (The LIGO Scientific Collaboration et al. 2016).

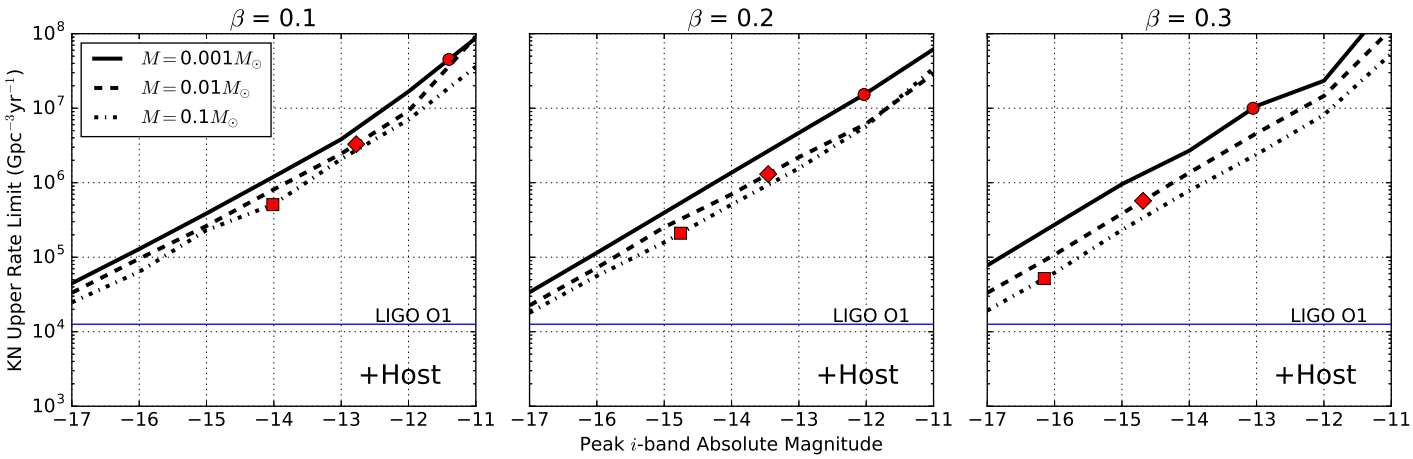

Figure 14. The same as Fig. 13, except using `DiffImg` efficiencies accounting for the SB anomaly.

6. DISCUSSION

The upper limits on the KN rate set in our analysis are a few orders of magnitude above other estimates. The LIGO Collaboration set an upper limit on the BNS merger rate of 1.26×10^4 yr^{-1}Gpc^{-3} (The LIGO Scientific Collaboration et al. 2016), and Fong et al. (2015) estimate a true SGRB rate of 270^{+1580}_{-180} yr^{-1}Gpc^{-3}. Although the limits presented in this work are not the most stringent, our analysis is independent of and consistent with other experiments and it directly sets limits on KN-like optical emission.

A key finding in this work is that the SB subtraction anomaly and SN background signals are major limitations in using DECam to search for KNe. Based on our results, the efficiency loss from underlying host galaxies reduces the KN search sensitivity by a factor of 3 relative to KNe with an undetected host. Further study is also required to determine the sensitivity reduction within the LIGO 80-170 Mpc range (Abbott et al. 2016d). A small part of this reduced sensitivity is from Poisson noise, and cannot be reduced. The major source of degradation, however, is from the difference imaging software. This software was developed and optimized several years ago to discover high-redshift SNe, with little motivation to find faint sources on bright galaxies. With new motivation to find EM counterparts to LIGO-triggered GW events, the software optimizations need to be revisited with the goal of improving the KN efficiency.

The cuts needed to adequately remove SNe and other backgrounds remove about half of the KN triggers, as shown in Tables 1 and 2. Our analysis reduced the predicted SN background to 1.1 ± 0.2 events in our sample, but this background will increase with higher search sensitivity or with looser cuts. While the MJD range of SN explosions will be reduced in follow-up to LIGO triggers, analysis cuts would be relaxed for two reasons. First, to maximize area coverage, only i and z band were used in Soares-Santos et al. (2016) (no g, r), which removes veto cuts 4 and 5 from § 4.1. Second, there is no pre-trigger veto unless there are serendipitous observations such as in Cowperthwaite et al. (2016). They detected a red, rapidly declining source in the follow-up observations of GW151216 (Abbott et al. 2016a) with DEcam, but the source was vetoed since the Pan-STARRS Survey for Transients had identified it 94 days before the GW event. These relaxed cuts are likely to increase backgrounds.

Our analysis also establishes the need for robust asteroid rejection. The $\sim$ 5-minute separation between i and z exposures in our shallow-field sample (75 minutes for deep fields) is adequate for removing asteroids. To maximize the area of future GW follow-up observations, shorter i and z exposure times may be used, and therefore consecutive $i + z$ exposures would be separated by less than the 5 minutes in our DES-SN sample. To reduce asteroid contamination, a minimum time between i and z exposures should be considered, such as observing several i-band pointings before repeating in the z-band. The additional telescope slews may cost more overhead than the extra filter changes, and thus EM programs would benefit from a more rigorous analysis of observation strategies.

For future surveys searching for KNe, our analysis has a few important implications. One implication is an estimate of the KN rate limits that could be set with other surveys. The Large Synoptic Survey Telescope (LSST), for example, will image $\sim$ 1000 times more sky area than DES-SN, suggesting that LSST could further constrain the rate limits presented here if the LSST cadence is comparable to that of DES-SN (LSST Science Collaboration et al. 2009). Our analysis also shows that multi-band observations will be essential for robust background rejection. Lastly, further optimizations to the survey cadence and temporal spacing of exposures could be made to maximize the gains from a KN search. In particular, a faster cadence would maximize the chance for detection of short-lived KNe, and a minimum time between the i and z exposures is needed to limit asteroid contamination.

7. CONCLUSION

We have presented a search for KNe in the Dark Energy Survey supernova fields. Simulations of kilonovae and supernovae were performed to tune cuts, determine search efficiency, and assess background levels. In our analysis of the first two DES-SN seasons, we find no KN candidates and set the first untriggered optical search limits on the rate of BK13-like KN events. The most serious issue for our search is a factor of $\sim$ 3 loss in sensitivity due to difference-imaging for faint sources on bright galaxies. For the brightest KNe considered in this analysis, our limits are comparable to the limits set by the LIGO collaboration from gravitational wave observations (The LIGO Scientific Collaboration et al. 2016). During the course of our analysis, Barnes et al. (2016) updated the BK13 KN light curve models. The absolute magnitudes of these updated models are fainter compared to BK13, but are well within the range considered in our analysis. This work sets the stage for further KN searches with DECam and other large-field-of-view telescopes such as Pan-STARRS1 or Large Synoptic Survey Telescope.

8. ACKNOWLEDGMENTS

We would like to thank Dan Kasen for providing us with the BK13 light curves. We also gratefully acknowledge support from the Kavli Institute for Cosmological Physics at the University of Chicago. Z.D. is supported by the NSF Graduate Research Fellowship Program, grant DGE-1144082. R.J.F. is supported in part by NSF grant AST-1518052 and from a fellowship from the Alfred P. Sloan Foundation.

Funding for the DES Projects has been provided by the U.S. Department of Energy, the U.S. National Science Foundation, the Ministry of Science and Education of Spain, the Science and Technology Facilities Council of the United Kingdom, the Higher Education Funding Council for England, the National Center for Supercomputing Applications at the University of Illinois at Urbana-Champaign, the Kavli Institute of Cosmological Physics at the University of Chicago, the Center for Cosmology and Astro-Particle Physics at the Ohio State University, the Mitchell Institute for Fundamental Physics and Astronomy at Texas A&M University, Financiadora de Estudos e Projetos, Fundação Carlos Chagas Filho de Amparo à Pesquisa do Estado do Rio de Janeiro, Conselho Nacional de Desenvolvimento Científico e Tecnológico and the Ministério da Ciência, Tecnologia e In-

ovação, the Deutsche Forschungsgemeinschaft and the Collaborating Institutions in the Dark Energy Survey.

The Collaborating Institutions are Argonne National Laboratory, the University of California at Santa Cruz, the University of Cambridge, Centro de Investigaciones Energéticas, Medioambientales y Tecnológicas-Madrid, the University of Chicago, University College London, the DES-Brazil Consortium, the University of Edinburgh, the Eidgenössische Technische Hochschule (ETH) Zürich, Fermi National Accelerator Laboratory, the University of Illinois at Urbana-Champaign, the Institut de Ciències de l'Espai (IEEC/CSIC), the Institut de Física d'Altes Energies, Lawrence Berkeley National Laboratory, the Ludwig-Maximilians Universität München and the associated Excellence Cluster Universe, the University of Michigan, the National Optical Astronomy Observatory, the University of Nottingham, The Ohio State University, the University of Pennsylvania, the University of Portsmouth, SLAC National Accelerator Laboratory, Stanford University, the University of Sussex, Texas A&M University, and the OzDES Membership Consortium.

The DES data management system is supported by the National Science Foundation under Grant Number AST-1138766. The DES participants from Spanish institutions are partially supported by MINECO under grants AYA2012-39559, ESP2013-48274, FPA2013-47986, and Centro de Excelencia Severo Ochoa SEV-2012-0234. Research leading to these results has received funding from the European Research Council under the European Union's Seventh Framework Programme (FP7/2007-2013) including ERC grant agreements 240672, 291329, and 306478.

This work was supported in part by the Kavli Institute for Cosmological Physics at the University of Chicago through grant NSF PHY-1125897 and an endowment from the Kavli Foundation and its founder Fred Kavli.

REFERENCES

Abbott, B. P., Abbott, R., Abbott, T. D., et al. (2016a). Gw151226: Observation of gravitational waves from a 22-solar-mass binary black hole coalescence. *Phys. Rev. Lett.*, 116:241103.

Abbott, B. P., Abbott, R., Abbott, T. D., et al. (2016b). Localization and broadband follow-up of the gravitational-wave transient gw150914. *The Astrophysical Journal Letters*, 826(1):L13.

Abbott, B. P., Abbott, R., Abbott, T. D., et al. (2016c). Observation of Gravitational Waves from a Binary Black Hole Merger. *Physical Review Letters*, 116(6):061102.

Abbott, B. P., Abbott, R., Abbott, T. D., et al. (2016d). Prospects for Observing and Localizing Gravitational-Wave Transients with Advanced LIGO and Advanced Virgo. *Living Reviews in Relativity*, 19.

Annis, J., Soares-Santos, M., Berger, E., et al. (2016). A Dark Energy Camera Search for Missing Supergiants in the LMC After the Advanced LIGO Gravitational Wave Event GW150914. *ArXiv e-prints*.

Barnes, J. and Kasen, D. (2013). Effect of a High Opacity on the Light Curves of Radioactively Powered Transients from Compact Object Mergers. *ApJ*, 775:18.

Barnes, J., Kasen, D., Wu, M.-R., and Mart'inez-Pinedo, G. (2016). Radioactivity and thermalization in the ejecta of compact object mergers and their impact on kilonova light curves. *ArXiv e-prints*.

Berger, E., Fong, W., and Chornock, R. (2013). An r-process Kilonova Associated with the Short-hard GRB 130603B. *Astrophys. J.*, 774:L23.

Bernstein, J. P., Kessler, R., Kuhlmann, S., et al. (2012). Supernova Simulations and Strategies for the Dark Energy Survey. *ApJ*, 753:152.

Bilicki, M., Jarrett, T. H., Peacock, J. A., Cluver, M. E., and Steward, L. (2014). Two Micron All Sky Survey Photometric Redshift Catalog: A Comprehensive Three-dimensional Census of the Whole Sky. *ApJS*, 210:9.

Bonnett, C., Troxel, M. A., Hartley, W., et al. (2015). Redshift distributions of galaxies in the DES Science Verification shear catalogue and implications for weak lensing. *ArXiv e-prints*.

Cowperthwaite, P. S. and Berger, E. (2015). A Comprehensive Study of Detectability and Contamination in Deep Rapid Optical Searches for Gravitational Wave Counterparts. *ApJ*, 814:25.

Cowperthwaite, P. S., Berger, E., Soares-Santos, M., et al. (2016). A DECam Search for an Optical Counterpart to the LIGO Gravitational Wave Event GW151226. *ArXiv e-prints*.

Dalal, N., Holz, D. E., Hughes, S. A., and Jain, B. (2006). Short GRB and binary black hole standard sirens as a probe of dark energy. *Phys. Rev. D*, 74(6):063006.

Diehl, H. T., Neilsen, E., Gruendl, R., et al. (2016). The dark energy survey and operations: years 1 to 3.

Dilday, B., Kessler, R., Frieman, J. A., et al. (2008). A Measurement of the Rate of Type Ia Supernovae at Redshift z Appl. Phys. 0.1 from the First Season of the SDSS-II Supernova Survey. *ApJ*, 682:262–282.

Drout, M. R., Chornock, R., Soderberg, A. M., et al. (2014). Rapidly Evolving and Luminous Transients from Pan-STARRS1. *ApJ*, 794:23.

Flaugher, B., Diehl, H. T., Honscheid, K., et al. (2015). The Dark Energy Camera. *AJ*, 150:150.

Fong, W., Berger, E., Margutti, R., and Zauderer, B. A. (2015). A Decade of Short-duration Gamma-Ray Burst Broadband Afterglows: Energetics, Circumburst Densities, and Jet Opening Angles. *ApJ*, 815:102.

Goldstein, D. A., DAndrea, C. B., Fischer, J. A., et al. (2015). Automated Transient Identification in the Dark Energy Survey. *AJ*, 150:82.

Gupta, R. R., Kuhlmann, S., Kovacs, E., et al. (2016). Host Galaxy Identification for Supernova Surveys. *ArXiv e-prints*.

Guy, J., Sullivan, M., Conley, A., et al. (2010). The Supernova Legacy Survey 3-year sample: Type Ia supernovae photometric distances and cosmological constraints. *A&A*, 523:A7.

Ji, A., Frebel, A., Chiti, A., and Simon, J. (2016). R-process enrichment from a single event in an ancient dwarf galaxy. *Nature*, 531(7596):610–613.

Jin, Z.-P., Fan, Y.-Z., and Wei, D.-M. (2016). An r-process macronova/kilonova in GRB 060614: evidence for the merger of a neutron star-black hole binary. In *European Physical Journal Web of Conferences*, volume 109 of *European Physical Journal Web of Conferences*, page 08002.

Kessler, R., Bassett, B., Belov, P., et al. (2010). Results from the Supernova Photometric Classification Challenge. *PASP*, 122:1415–1431.

Kessler, R., Bernstein, J. P., Cinabro, D., et al. (2009). SNANA: A Public Software Package for Supernova Analysis. *PASP*, 121:1028–1035.

Kessler, R., Guy, J., Marriner, J., et al. (2013). Testing Models of Intrinsic Brightness Variations in Type Ia Supernovae and Their Impact on Measuring Cosmological Parameters. *ApJ*, 764:48.

Kessler, R., Marriner, J., Childress, M., and The DES Collaboration (2015). The Difference Imaging Pipeline for the Transient Search in the Dark Energy Survey. *AJ*, 150:172.

Li, L.-X. and Paczyński, B. (1998). Transient Events from Neutron Star Mergers. *ApJ*, 507:L59–L62.

Li, W., Chornock, R., Leaman, J., et al. (2011). Nearby supernova rates from the lick observatory supernova search ? iii. the rate?size relation, and the rates as a function of galaxy hubble type and colour. *Monthly Notices of the Royal Astronomical Society*, 412(3):1473–1507.

Lippuner, J. and Roberts, L. F. (2015). r-process Lanthanide Production and Heating Rates in Kilonovae. *ApJ*, 815:82.

LSST Science Collaboration, Abell, P. A., Allison, J., et al. (2009). LSST Science Book, Version 2.0. *ArXiv e-prints*.

Metzger, B. D. and Berger, E. (2012). What is the Most Promising Electromagnetic Counterpart of a Neutron Star Binary Merger? *Astrophys. J.*, 746:48.

Metzger, B. D. and Fernández, R. (2014). Red or blue? A potential kilonova imprint of the delay until black hole formation following a neutron star merger. *MNRAS*, 441:3444–3453.

Narayan, R., Paczynski, B., and Piran, T. (1992). Gamma-ray bursts as the death throes of massive binary stars. *ApJ*, 395:L83–L86.

Paczynski, B. (1986). Gamma-ray bursters at cosmological distances. *ApJ*, 308:L43–L46.

Rest, A., Scolnic, D., Foley, R. J., et al. (2014). Cosmological Constraints from Measurements of Type Ia Supernovae Discovered during the First 1.5 yr of the Pan-STARRS1 Survey. *ApJ*, 795:44.

Sako, M., Bassett, B., Becker, A. C., et al. (2014). The Data Release of the Sloan Digital Sky Survey-II Supernova Survey. *ArXiv e-prints*.

Schutz, B. (1986). Determining the Hubble constant from gravitational wave observations. *Nature*, 323:310–311.

Shen, K. J., Kasen, D., Weinberg, N. N., Bildsten, L., and Scannapieco, E. (2010). Thermonuclear .ia supernovae from helium shell detonations: Explosion models and observables. *The Astrophysical Journal*, 715(2):767.

Soares-Santos, M., Kessler, R., Berger, E., et al. (2016). A Dark Energy Camera Search for an Optical Counterpart to the First Advanced LIGO Gravitational Wave Event GW150914. *ArXiv e-prints*.

Tanaka, M. and Hotokezaka, K. (2013). Radiative transfer simulations of neutron star merger ejecta. *The Astrophysical Journal*, 775(2):113.

Tanvir, N. R., Levan, A. J., Fruchter, A. S., et al. (2013). A 'kilonova' associated with the short-duration γ-ray burst GRB 130603B. *Nature*, 500:547–549.

The LIGO Scientific Collaboration, the Virgo Collaboration, Abbott, B. P., Abbott, R., Abbott, T. D., et al. (2016). Upper limits on the rates of binary neutron star and neutron-star–black-hole mergers from Advanced LIGO's first observing run. *ArXiv e-prints*.